APPLIED PHYSICS

Tunable plasmonic superchiral light for ultrasensitive detection of chiral molecules

Aritra Biswas[1,2], Pablo Cencillo-Abad[1], Muhammad W. Shabbir[1], Manobina Karmakar[1], Debashis Chanda[1,2,3]*

The accurate detection, classification, and separation of chiral molecules are pivotal for advancing pharmaceutical and biomolecular innovations. Engineered chiral light presents a promising avenue to enhance the interaction between light and matter, offering a noninvasive, high-resolution, and cost-effective method for distinguishing enantiomers. Here, we present a nanostructured platform for surface-enhanced infrared absorption–induced vibrational circular dichroism (VCD) based on an achiral plasmonic system. This platform enables precise measurement, differentiation, and quantification of enantiomeric mixtures, including concentration and enantiomeric excess determination. Our experimental results exhibit a 13 orders of magnitude higher detection sensitivity for chiral enantiomers compared to conventional VCD spectroscopic techniques, accounting for respective path lengths and concentrations. The tunable spectral characteristics of this achiral plasmonic system facilitate the detection of a diverse range of chiral compounds. The platform's simplicity, tunability, and exceptional sensitivity holds remarkable potential for enantiomer classification in drug design, pharmaceuticals, and biological applications.

INTRODUCTION

Nature favors chirality, the property describing objects whose mirror image is nonsuperimposable. Handedness is omnipresent in the universe: Shells, shoes, scissors, galaxies, and DNA are just a few examples. In the molecular realm, pairs of isomers corresponding to the two mirror images of a molecule are called enantiomers—same molecule with opposite handedness. In many instances, while one enantiomer is safe to use as a commercial commodity, the opposite enantiomer can be toxic (*1*). Thalidomide ($C_{13}H_{10}N_2O_4$) is arguably the most infamous example, which was originally introduced in the 1960s to alleviate morning sickness in pregnant women. Follow-up studies after occurrences of severe birth defects revealed that only the clockwise (+) enantiomer is a sedative, while its anti-clockwise (−) isomer is degenerative—responsible for the birth defects (*2*). Over the years, pharmaceutical and medical research demanded simple, robust, and accurate methods for chiral discrimination. Among these methods, transmission-based vibrational circular dichroism (VCD) measurements have been the gold standard for decades (*3*). Both dispersive and Fourier transform spectroscopy–based VCD have shown to distinguish molecular handedness. The biggest downside of such measurements is that a high concentration of molecules is required to achieve a measurable differential absorption signal. Furthermore, typical absorption dissymmetry signals are of the order of 10^{-7} to 10^{-5}, lacking signal-to-noise ratios required for accurate circular dichroism (CD) measurements.

Being a transverse wave, light can carry angular momentum (*4*, *5*). In particular, elliptically polarized light exhibits time dynamic rotation while traveling in space, showing two handedness determined by the direction of the temporal rotation around the axis of propagation. For such light, the principle of conservation of angular momentum results in a conserved property (*6*) called chirality (*7*, *8*). Chirality (C), or optical chiral density, is an electromagnetic pseudo-scalar quantity whose magnitude depends on the handedness of the polarization. For a monochromatic source traveling with angular frequency ω, the chiral density as a function of the position is given by (*7*, *9*)

$$C = -\frac{\varepsilon_0 \omega}{2} \mathrm{Im}(\mathbf{E}^* \bullet \mathbf{B}) \quad (1)$$

where **E** and **B** are the complex time-dependent electric and magnetic field vectors and ε_0 is the vacuum permittivity. For general free-space propagating wave, optical chiral density C is maximum for circularly polarized light (C_{CPL}), having orthogonal field vectors with equal magnitudes and a $\pm\pi/2$ phase. Enabled by the development of novel micro- and nanofabrication technologies, several classes of new artificial optical structures have been shown to enhance C, with some proposed architecture exhibiting regions with artificially enhanced C more than that of free-space CPL ($|C/C_{CPL}| > 1$). This phenomenon, known as superchiral light (*7*, *8*, *10*), has drawn researchers' attention in recent times for its potential in manipulating chiral light-matter interactions. Several such proposed systems rely on chiral photonic (*11*–*13*) and plasmonic surfaces (*10*, *14*–*17*) that produce superchiral near fields (*18*–*21*) at resonance. However, the structural chirality of these systems inherently results in strong far-field CD signals that overshadows the weak molecular CD signals produced by the chiral light-matter interactions in the near-field, making them inefficient for chiral molecule detection and sensing. Moreover, such nanostructures (*22*–*27*) suffer from spatial inhomogeneity in the handedness of the chiral near-field, further limiting the overall molecular CD. Therefore, a strong design requirement for the sensitive detection of weak molecular CD signals is to have structural achirality that would suppress the far-field CD from the nanostructure itself, as well as a uniform, single-handed chiral near-field in the entire probing volume (*28*, *29*).

Here, we demonstrate an achiral plasmonic system for sensitive detection and discrimination of chiral molecules. Because of the coherent interaction between degenerate plasmonic and photonic cavity modes, the system exhibits high-quality factor localized surface

[1]NanoScience Technology Center, University of Central Florida, 12424 Research Parkway Suite 400, Orlando, FL 32826, USA. [2]CREOL, The College of Optics and Photonics, University of Central Florida, 4304 Scorpius St., Orlando, FL 32816, USA. [3]Department of Physics, University of Central Florida, 4111 Libra Drive, Physical Sciences Bldg. 430, Orlando, FL 32816, USA.
*Corresponding author. Email: debashis.chanda@ucf.edu

plasmon resonances (LSPRs) with near perfect absorption (*30*–*32*). This system offers distinct advantages (*28*) compared to previously reported methodologies. On illumination with CPL, the surface exhibits simultaneous local enhancement of electromagnetic near-field and a single-handed superchiral field at resonance whose polarization handedness solely depends on the excitation handedness (*32*). Moreover, the nanostructure is geometrically achiral, thus generating zero far-field CD while concurrently displaying near-field optical chiral density enhancement on the surface. Hence, compared to previous attempts where inhomogeneous chiral near-field and structural CD diminishes chiral signal from molecules (*10*, *33*–*35*), this system enables the far-field CD signal to be purely generated by the adsorbed molecule. The design principles for the proposed handedness-preserving structure have been detailed in our prior research (*32*). The resonance can be shifted by altering geometrical parameters, consequently enabling superchiral field tunability. The system permits efficient chiral-light matter interaction for the detection of vibrational molecular chirality in the mid-infrared (MIR) domain relevant for multiple important applications including drug screening and protein conformational changes (*32*). Further, when the system LSPR resonance overlaps strongly with the molecular absorption, the measured far-field CD is greatly enhanced even for very low concentration of analytes. We show that our system can selectively detect and distinguish several concentrations of enantiomers and can also discriminate and determine various enantiomeric excesses. Present bulk liquid–based conventional VCD measure absorption dissymmetry (right versus left molecules) values within the range of 10^{-7} to 10^{-5} μm^{-1} for path length (L) of millimeter to centimeter range and molar concentrations in the order of 10^{-1} M (*36*). In contrast, our thin-film approach measures dissymmetry factors ($g \sim 10^{-2}$ to 10^{-1}) even for concentrations as low as 50 μM based on extremely low volumes of a few microliters. Accounting for both path length and concentration, there is an estimated 13 orders of magnitude enhancement of the normalized dissymmetry factor ($g_{norm} = g/L$ per M) compared to present state-of-the-art method. The sensors are easy to fabricate based on simple large area nanoimprinting technique and can be reused after simple cleaning steps. Such a system has great potential in pharmaceutical and drug industries where highly sensitive, high-throughput, and low-cost enantiomeric purity determination is critically important.

RESULTS

Figure 1A shows the proposed cavity-coupled achiral plasmonic system (*32*). The top surface consists of an array of gold hole-disk arranged in a square lattice. This two-dimensional (2D) arrangement generates inherent localized surface plasmon (LSP) modes. The lattice array is stacked on top of an underlying silicon dioxide (SiO_2) cavity above a gold back mirror. Figure 1B shows the scanning electron microscopy image of the top surface and the cross-sectional view of the plasmonic system. The cavity generates Fabry-Perot modes that hybridize the LSP modes of the hole-disk arrangement, resulting in the modification of the overall response (*30*–*32*, *37*). This coupled system produces several higher order modes due to hybrid LSPRs spread over a large spectral range from visible to MIR frequencies. For our study, we focus on the lowest order mode located in the 4- to 7-μm infrared domain to detect chiral drug molecules based on their vibrational absorption resonances. Because of the unique design, the response can be tuned to cover the whole MIR spectral range by changing lattice and cavity parameters (see fig. S1, A and B) (*38*). At the LSPR wavelength, enhanced electric and magnetic modes are simultaneously generated in the near-field of the hole-disk system as can be seen in fig. S1D. Most of the strong electric field enhancement is localized at the bottom disk region, while a strong magnetic mode enhancement is observed at the top-hole region. When circularly polarized excitation is incident on the system, the near-field modes begin to rotate in time and space on the hole-disk array due to temporally rotating nature of the circular polarization. Coupling between these spatially displaced rotating modes, and further hybridization with the cavity modes leads to a strong and uniform local optical chiral density enhancement (superchirality) at the near-field due to the simultaneous enhancements of **E** and **B** fields in the overlap regions. Figure 1D shows the finite-difference time-domain (FDTD) predicted normalized optical chiral density (with respect to CPL) in the near-field of the system at the lowest order LSPR wavelength (5.41 μm in this case). The observed chiral field distribution offers distinct advantages: (i) The superchiral field is localized near and above the top-hole region of the system, where most of the molecules adsorb, hence increasing the surface area of interaction; (ii) the enhanced field is uniform allowing maximum molecule-chiral near-field interactions; and (iii) it has the same sign as the excitation CPL enabling easy control of the chiral near-field based on the handedness of the molecule.

The unequal light-matter interaction is quantified by the dissymmetry factor (g), given by

$$g = 2\left(\frac{A^{R} - A^{L}}{A^{R} + A^{L}}\right) \tag{2}$$

where $A^{(R/L)}$ is the overall rate of absorption or absorbance in the presence of right/left circularly polarized (RCP or LCP) excitation. The absorption rate of a randomly oriented chiral molecule excited with a monochromatic right/left-handed polarized light is given by (*7*)

$$A^{(R/L)} = \frac{\omega}{2}(\alpha'' |\mathbf{E}|^2 + \chi'' |\mathbf{B}|^2) \pm G''\omega \ \mathrm{Im}(\mathbf{E}^* \bullet \mathbf{B}) \tag{3}$$

where ω is the angular frequency of the EM light and α″, χ″, and G'' are the imaginary parts of electric polarizability, magnetic susceptibility, and the mixed magnetoelectric polarizability of the chiral molecule. Inserting Eq. 3 in the expression for g in Eq. 2 and using the definition of chirality C from Eq. 1, the dissymmetry factor becomes (*7*, *8*)

$$g = -\left(\frac{G''}{\alpha''}\right)\left(\frac{8C}{\omega\varepsilon_0 |\mathbf{E}|^2}\right) \tag{4}$$

where the contribution from the magnetic susceptibility for a non-magnetic molecule is neglected. The expression for the dissymmetry factor is given by the product of the optical properties of the molecules (first term in parenthesis) and the ratio of the electromagnetic chirality (C) to the field enhancement (second term in parenthesis). The dissymmetry factor can then be either enhanced by increasing the molecular magnetoelectric polarizability (G''), which is a fixed natural quantity associated with molecules, or by enhancing the optical chiral density (C) of the near-field environment. In our case, this second term in parenthesis in Eq. 4 is what we have shown to enhance in our system's near field, which is the prime origin of the high enhancement in the dissymmetry that we observe in our measurements. Hence, to maximize dissymmetry,

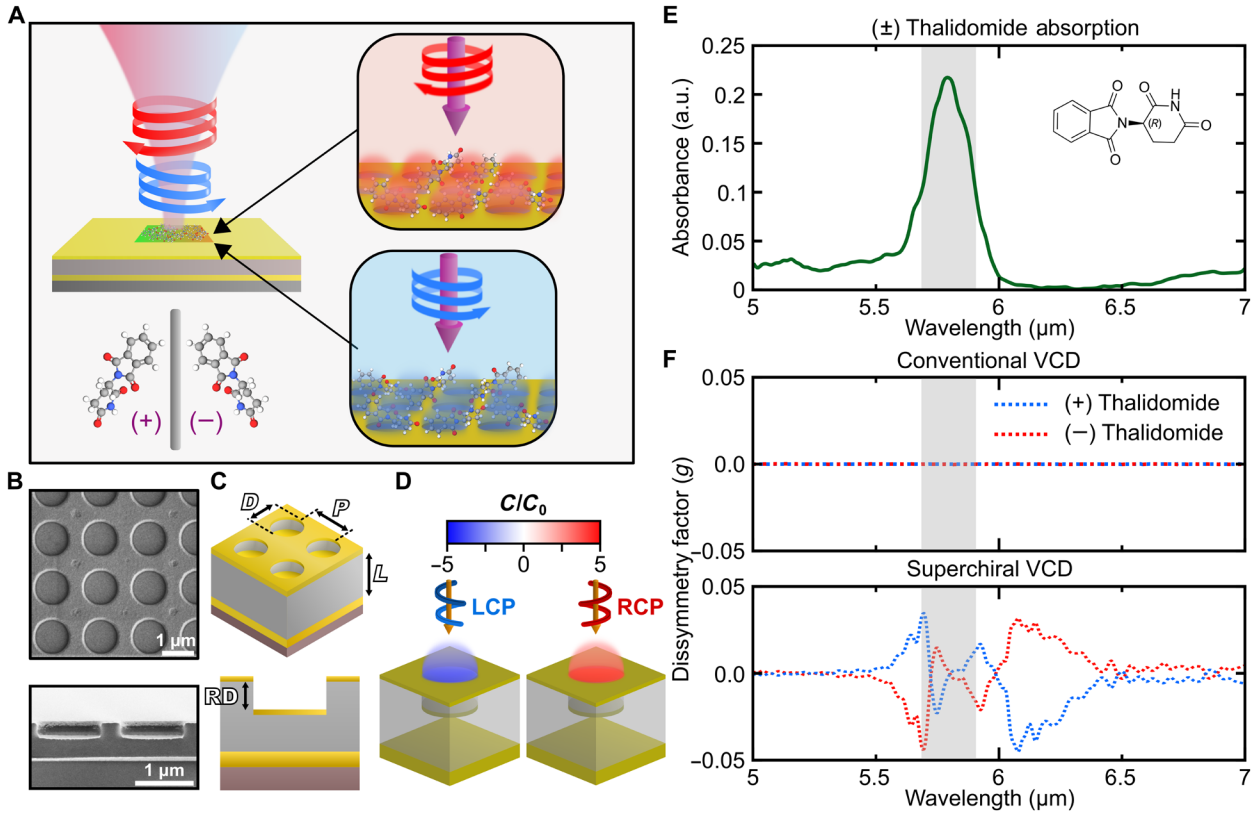

Fig. 1. Superchiral plasmonic sensor. (**A**) Schematic of the superchiral plasmonic sensor along with measurement protocol. (**B**) Scanning electron microscopy (SEM) images of the sensor showing periodic array of gold hole and disks (top) and the corresponding cross-sectional view (bottom). (**C**) Cartoon representation of the achiral plasmonic sensor showing the geometric parameters, periodicity (P = 1.74 μm), diameter (D = 1.06 μm), cavity thickness (L = 1 μm), and relief depth (RD = 0.3 μm). (**D**) FDTD predicted near-field chiral response over the hole-disk geometry. (**E**) Absorbance spectra of a (±) thalidomide thin film on gold measured with nano-FTIR. a.u., arbitrary units. (**F**) Comparison of dissymmetry factors measured using conventional VCD and proposed superchiral VCD for 1 mM thalidomide with an average coating thickness of 160 nm. Conventional VCD produced no signal, whereas superchiral VCD produced strong signal based on the same concentration.

one needs to find a region with simultaneous strong optical chiral density and a relatively low electric field enhancement. For the proposed system, most of the electric field enhancement is localized at the bottom disk region, while it is relatively low at the top-hole region (fig. S1E). Consequently, the top surface satisfies both conditions, resulting in a strong dissymmetry factor at resonance.

To demonstrate the applicability of our system in the determination of various concentrations and enantiomeric excesses of molecules, we selected thalidomide. Thalidomide is an immunomodulatory drug that exhibits structural chirality. Tragically, unaware of its toxic effects, it was routinely prescribed for alleviating morning sickness in pregnant women in the late 1950s and early 1960s. However, while one enantiomer of thalidomide (+) is a potent curing agent, the opposite handedness is a teratogen that can cause birth defects if consumed by pregnant women. Although it is banned for commercial use in several countries for many years, recent applications of thalidomide have received experimental approval and are being used in cancer and leprosy-treatment research (*39*–*41*). For the first set of experiments, enantiopure dilutions (solutions having one enantiomer) of thalidomide (±) (Sigma-Aldrich Co.) are prepared while keeping the overall molar concentration same. To maintain potency of enantiopure thalidomide, experiments are conducted within 24 hours of freshly made solutions. We target the thalidomide absorption band centered at 5.79 μm, corresponding to the C═O stretching vibrations. Figure 1E shows the absorption spectra of a thin film of adsorbed thalidomide on pristine gold layer for the desired spectral range, measured with a tip-based atomic force microscopy (AFM)–coupled nano–Fourier transform infrared (FTIR) system [Attocube (neaspec) GmbH, detailed measurement procedure is in the Materials and Methods] (*42*). The adsorbed film is approximately 160 nm in thickness. Films of such thicknesses are much smaller than the wavelength of infrared excitation; hence, they are spectrally unobservable in regular reflection-mode FTIR measurements. For strong CD enhancement, one major requirement is to have a strong overlap between the molecular absorption and the system's LSPR response. Figure 1F shows a comparison of the VCD signal for similar concentration of thalidomide measured using conventional VCD and the proposed superchiral VCD method. It is clear that superchiral VCD produces an enhancement in dissymmetry factor ($g \sim 10^{-2}$), whereas conventional VCD produced no distinguishable signal at the same scale bar. To ensure accurate measurement and minimize potential artifacts, separate baseline references were taken for LCP and RCP excitation. Taking a differential measurement of the coupled sensor-molecule system resulted in clear, distinct, and unambiguous data allowing for precise determination of the flipping of dissymmetry signs at resonance locations (Fig. 1 to 3).

To better understand the energy exchange between the plasmonic system and chiral molecules, we perform finite element method (FEM)–based simulations using COMSOL Multiphysics software. We modeled the system as a periodic 2D structure with a unit cell made up of one cavity-coupled hole-disk geometry, and a thin chiral molecular layer on the top surface. The chiral layer is modeled as a Lorentzian oscillator having a relative permittivity ϵ_r and an associated magnetoelectric (chiral) parameter κ (*25*, *43*–*46*). The parameter κ is a complex valued dimensionless quantity related to the mixed polarizability associated with magnetic-electric coupled mode. The parameters are taken as

$$\epsilon_r = \epsilon_{r0} - \gamma\left(\frac{1}{\hbar\omega - \hbar\omega_0 + i\Gamma} - \frac{1}{\hbar\omega + \hbar\omega_0 + i\Gamma}\right) \quad (5)$$

$$\kappa = \beta\left(\frac{1}{\hbar\omega - \hbar\omega_0 + i\Gamma} + \frac{1}{\hbar\omega + \hbar\omega_0 + i\Gamma}\right) \quad (6)$$

where ϵ_{r0} is the background relative permittivity, $\hbar$ is the reduced Planck's constant, ω_0 is the molecule's resonance frequency, and Γ is the damping constant. The parameters γ and β are coefficients that depend on the density and dipole moments of the chiral molecules (*46*, *47*) and are chosen appropriately to simulate the resonant chiral response. Here, a simple case of isotropic molecular layer is considered over the region of interest. For a large enough ensemble consisting of randomly oriented molecules, the layer can be considered as a uniform, homogeneous layer with an effective handedness. The permittivity and chiral parameter dispersion plot are shown in fig. S2. To simulate the opposite enantiomer response, we simply switch the sign of κ. To simulate chiral light-matter interaction, we choose electromagnetic quantities that incorporate bi-isotropic media (*27*, *33*, *44*, *46*–*49*) by making changes in the displacement field vector $\hat{\mathbf{D}}$ and the magnetic field vector $\hat{\mathbf{B}}$

$$\hat{\mathbf{D}} = \epsilon_r\epsilon_0\hat{\mathbf{E}} - \frac{i\kappa}{c}\hat{\mathbf{H}} \quad (7)$$

$$\hat{\mathbf{B}} = \mu_r\mu_0\hat{\mathbf{H}} + \frac{i\kappa}{c}\hat{\mathbf{E}} \quad (8)$$

where ϵ_r and ϵ_0 are the relative and vacuum permittivity, respectively, and μ_r and μ_0 are the relative and vacuum permeability, respectively. Because most naturally occurring molecules are nonmagnetic, we take μ_r to be one. Figure 2 (A and B) shows the simulated absorption and dissymmetry spectra for the three cases of (left) off-resonant, (middle) on-resonant, and (right) off-resonant overlap for the bare sensor (dashed lines) and with the chiral molecular layer (solid lines). A clear splitting in the spectra can be observed at the position of overlap between the plasmonic and the molecular absorption resonance as indicated by the gray bar, accompanied by a slight redshift. This is due to the coupling between the electromagnetically driven strong localized plasmon resonance mode and the weak molecular mode, leading to a plasmon-induced transparency (PIT) window (*50*–*53*). We define the PIT amplitude as the difference in peak absorption before and at the point of dip in the induced transparency

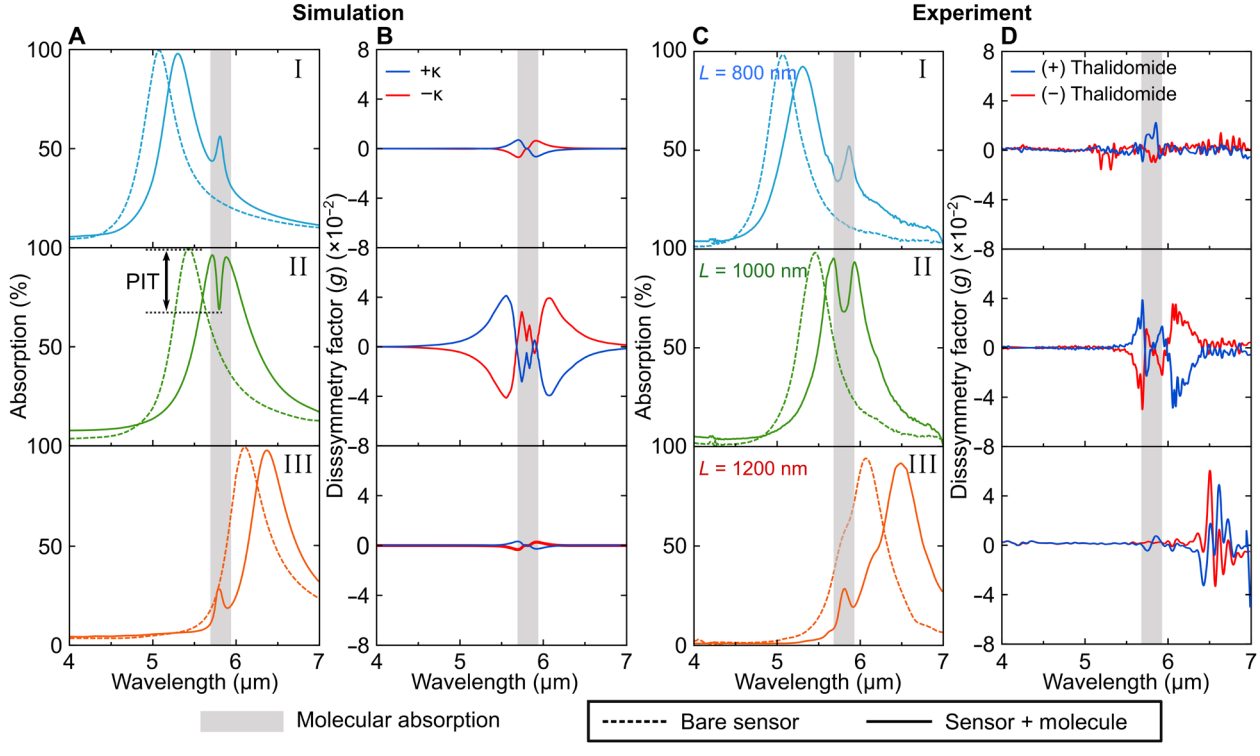

Fig. 2. PIT and dissymmetry factor. Simulated (**A** and **B**) and experimentally measured (**C** and **D**) three different cases of molecular absorption-plasmon resonance couplings and corresponding dissymmetry factors. The spectral location of the plasmon resonance with respect to the molecular resonance: (I) off-resonant to the left, (II) on-resonant overlap, and (III) off-resonant to the right. Substantial enhancement in the plasmon-induced transparency (PIT) and dissymmetry factor can be observed for the on-resonant condition (II). The PIT is defined as change in absorption at the overlap resonance.

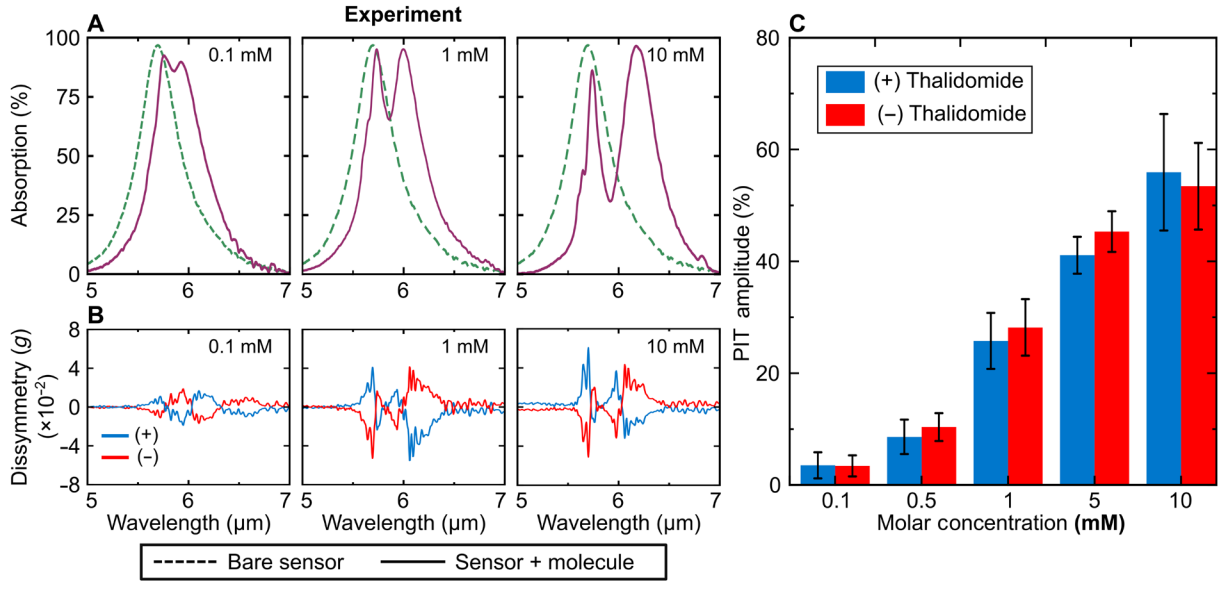

Fig. 3. Molecular concentration–dependent PIT and dissymmetry. (**A**) Sensor's spectral response before (dashed lines) and after (solid lines) molecular adsorption, showing PIT as a function of thalidomide concentration. Corresponding baseline corrected experimentally measured *g*-factors (**B**) and PIT amplitude (**C**) for different concentrations.

after molecular adsorption (Fig. 2A). The corresponding predicted dissymmetry factors (*g*) of both thalidomide enantiomers for the three cases are shown in Fig. 2B. Although all three cases show an induced transparency region at the position of overlap, the dissymmetry value is maximized and symmetric for the middle system where the plasmon resonance is overlapped with the molecular absorption resonance. Partial overlaps show considerably weaker dissymmetry, as seen in the weakly overlapping cases in Fig. 2B. To verify these FEM predictions of energy exchange between the plasmon mode and the molecule, three sensors having first-order LSPR responses at different wavelengths (left off-resonance, on-resonance, and right off-resonance) are fabricated. The sensors are coated with the same concentration of thalidomide. Surface topology measurement using tapping-mode AFM indicates an average thickness of 160 nm of the adsorbed layer (see Materials and Methods). The experimental absorption spectra for the three cases are shown in Fig. 2C before (dashed lines) and after (solid lines) molecular adsorption. Next, the VCD spectra for the molecule-plasmonic system are measured for the same concentration of both thalidomide enantiomers, shown in Fig. 2D. A good agreement between simulation (Fig. 2, A and B) and measurement (Fig. 2, C and D) can be observed. As predicted, we observe that the maximum overlap (middle case) exhibits the strongest dissymmetry—an indication of maximum chiral interaction. Notice that, in the middle case (on-resonance), there are two zero crossings (CD flip) in the dissymmetry spectra corresponding to the two absorption peaks generated across the induced transparency (Fig. 2, middle case). Therefore, the PIT also plays a role in determining the shape of the observed dissymmetry spectra. However, as the origin of the induced transparency stems from the energy exchange between two systems, it can be observed even without an induced chiral response (as in the case of linearly polarized light). Most of the fast oscillations in the experimental data (Fig. 2D) are due to the minute differences in the reflectance (thus, absorbance) spectra for LCP and RCP excitation that are due to slight thickness variations and cryo-cooled mercury-cadmium-telluride (MCT) detector noises. Furthermore, the observed noise within the spectral range of 6 to 7 μm in Fig. 2D (bottom) is ascribed to water absorption, a phenomenon that becomes accentuated in the presence of a resonance peak within this wavelength domain.

Next, we study the effect of increasing the molecular concentration of enantiopure thalidomide and observe the far-field spectral response of our system. As demonstrated in Fig. 2, we choose a sensor such that the molecule-plasmon resonance overlap is maximum (Fig. 2, middle case). Figure 3A shows the absorption spectra of the plasmonic sensors before (dashed lines) and after (solid lines) adsorption of thalidomide at different concentrations. Clearly, the degree of PIT increases with concentration. There is a slight redshift of the response (due to the increase in the surrounding refractive index with concentration), but the LSPR position is not so much affected even with subsequent increase in concentration. Figure 3B shows the corresponding spectral dissymmetry values for the various concentrations in Fig. 3A, which clearly shows an increasing trend in the degree of dissymmetry. The PIT amplitudes for different molar concentrations of pure thalidomide enantiomers are shown in Fig. 3C. It is evident that the PIT amplitude exhibits a linear relationship with concentration for both enantiomers, thereby offering a reliable measure of the absolute concentration.

As mentioned before, when the molecular absorption overlaps strongly with the plasmonic mode, the dissymmetry value is substantially higher than the weakly or nonoverlapping cases (Fig. 2). Figure 4A shows the maximum dissymmetry values for different concentrations of enantiopure thalidomide. The sign of dissymmetry value is chosen as the first nonzero rise in dissymmetry factor, for example, (−) thalidomide starts with a decrease in its dissymmetry factor value before increasing, hence a negative sign and vice versa. As expected, an increase in maximum dissymmetry value is observed with increasing concentration. The lowest reliably measured

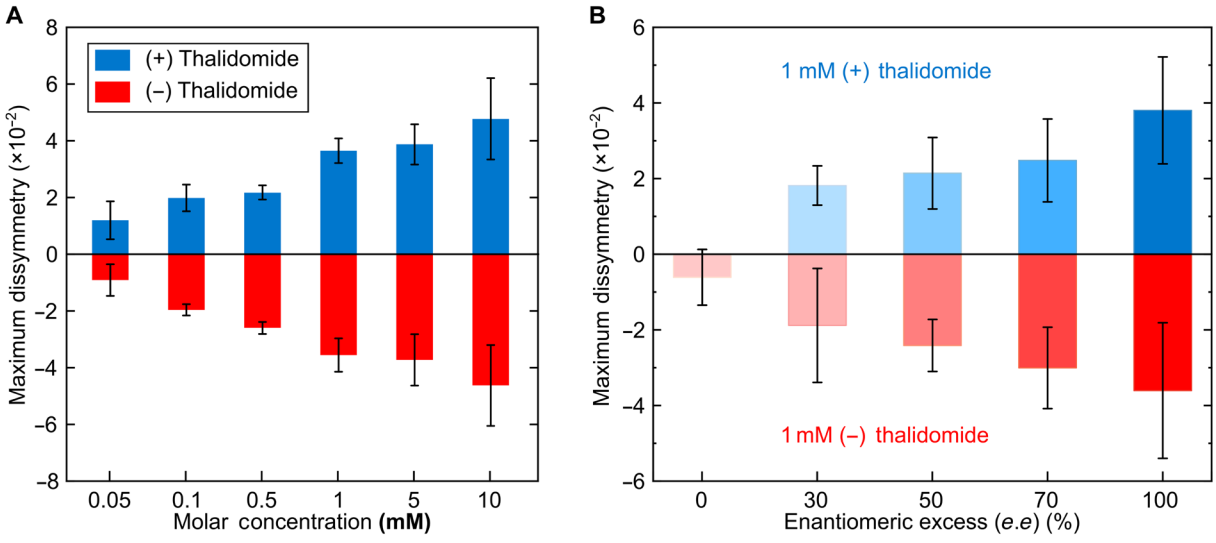

Fig. 4. Enantiopure and enantiomeric excess determination. (**A**) Bar plot of maximum dissymmetry for different concentrations of adsorbed enantiopure thalidomide. (**B**) Maximum observed dissymmetry for different enantiomeric excesses of (+) and (−) thalidomide. The concentration during *e.e* measurement is kept at 1 mM.

concentration is 50 μM (see Fig. 4A) for a maximum dissymmetry factor of 10^{-2}. In comparison, conventional VCD measures dissymmetry factors in range of 10^{-7} to 10^{-5} for typical millimeter- to centimeter-range path lengths (L) for 0.1 M range concentration (M) (*36*). Thus, upon normalization with respect to path length and concentration (g/L per M), our results demonstrate a 13 orders of magnitude enhancement in contrast {relative enhancement factor = [our normalized g (g/L per M)]/[conventional normalized g (g/L per M)] = (10^{-2}/50 μM/160 nm)/(10^{-7}/0.1 M/1 cm) ~ 10^{13}}.

For enantiopure molecules, one can discern a linear correlation between absolute concentration and both the PIT amplitude and the maximum dissymmetry signal. However, because of several environmental factors and manufacturing limitations, most of the naturally encountered chiral drugs exist as a mixture of enantiomers, and there is a huge need for quantifying enantiomeric purity (*1*). The enantiomeric excess (*e.e*) is used as a measure of purity of an enantiomer and is defined as

$$e.e = \left(\frac{n_+ - n_-}{n_+ + n_-}\right) \tag{9}$$

where n_+ and n_- are the moles of right and left enantiomers, respectively. In the next study, different enantiomeric excesses of thalidomide are prepared and adsorbed to the sensor surface. The overall molar concentration for all *e.e* solutions are kept the same, as 1 mM. Figure 4B shows the maximum dissymmetry values for different enantiomeric excesses of thalidomide. A linear trend is observed in their maximum dissymmetry factor values as it saturates at the maximum value of about 4×10^{-2}, as determined for 1 mM enantiopure thalidomide. However, we observe that the PIT amplitudes for all the *e.e* solutions are similar, indicating that the induced transparency-based splitting only depends on the molecular concentration as can be seen in Fig. 3C. Hence, a racemic {50% (+)/50% (−)} solution of enantiomers would have a noticeable PIT amplitude (see Fig. 3C for 1 mM concentration) but no dissymmetry value as seen in Fig. 4B for $e.e = 0$. This is the first such reported measurement of enantiomeric excesses to determine purity of any random enantiomeric mixture. An ultralow enantiomeric excesses detection sensitivity will allow accurate chiral molecule synthesis and life-saving drug design where enantiomeric purity and mixture play a critical role.

DISCUSSION

We demonstrate a nanostructured platform on the basis of an achiral plasmonic system that can detect and determine concentrations and enantiomeric excesses of chiral molecules. The symmetry of the sensor surface supresses any asymmetrical far-field optical response from the device itself, thereby eliminating the need for two mirror-imaged sensors. On excitation with CPL, an enhanced, homogenous, and local optical chiral density is generated whose handedness is controlled by the excitation handedness. Moreover, the asymmetry in far-field response as a result of molecular adsorption is entirely due to near-field coupling of the molecule-sensor resonance. We experimentally demonstrated a measure of the absolute concentration using the PIT amplitude and also exhibit detection of ultralow concentration as low as 50 μM and an effective path length of 160 nm for enantiomeric molecules with a maximum dissymmetry value of about 10^{-2}. An objective comparison with conventional far-field VCD measurement techniques having typically macroscopic path lengths (L) and moderate-to-high concentration ranges (~0.1 M) reveals a 13 orders of magnitude enhancement in detection sensitivity, when normalized with regard to path length and concentration.

Furthermore, the resonance response of the system can be tuned by simple parametric changes, which, in turn, changes the spectral location of the local optical chiral density, thereby enabling the detection and determination of a wide array of chiral molecules. Overall, the robustness, ease of fabrication, and fast measurement make it an ideal platform for an on-chip surface-enhanced ultrasensitive chirality detection tool for biomedical research and pharmaceutical industries.

MATERIALS AND METHODS

Sensor fabrication

A master pattern consisting of nanohole arrays is used to make a stamp mold made of polydimethylsiloxane (PDMS), which will be used for nanoimprinting in a later stage. Microscope glass slides are cut and cleaned with acetone, isopropyl alcohol (IPA), and deionized water, respectively, followed by drying with inert nitrogen and baking at 100°C for 10 min. A 5-nm titanium (Ti) adhesion layer, followed by 100-nm gold film, which acts as a back mirror, is deposited on the substrate by standard electron beam (e-beam) evaporation. This is followed by another 5-nm Ti adhesion layer. An amorphous SiO_2 thick layer is deposited by e-beam evaporation, which defines the optical cavity. Depending on the thickness required, several different cavities were prepared. A negative-photoresist SU-8 2000.5 (Kayaku Adv. Materials) is spin-coated on the substrates. The pattern is then thermally nanoimprinted on the photoresist with the PDMS stamp mold followed by ultraviolet curing. The nanohole pattern is then transferred onto the SiO_2 cavity by reactive ion etching in an Ar/CHF_3 environment at a 2:3 gas ratio. The etch recipe has been optimized to give excellent vertical side walls with a relief depth (RD) of 300 nm. This is followed by an e-beam deposition of 3-nm Ti/ 30 nm Au to create the top hole-disk structure, which finally concludes the fabrication process.

Chiral molecule preparation and adsorption

Both enantiomers of thalidomide (≥98% purity) (no. T150-10MG/no. T151-10MG) and dimethyl sulfoxide (DMSO) solvent (no. 276855-1 L) have been purchased from Sigma-Aldrich. The two thalidomide molecules are separately diluted in 100 µl of DMSO, a commonly used polar aprotic solvent, to prepare an initial 10 mM solutions, which were further serially diluted to prepare subsequent lower concentrations. Next, we prepared different enantiomeric excesses (*e.e*%) of both (+) and (−) thalidomide, from 100, 70, 50, 30, and 0% for each enantiomer. If n_+ and n_- are moles for (+) and (−) enantiomers, respectively, the *e.e*% for the (+) enantiomer is given by

$$e.e\,\% = \left(\frac{n_+ - n_-}{n_+ + n_-}\right) * 100 \tag{10}$$

The molarity M is related to moles n as

$$M = \frac{n}{V} \tag{11}$$

If the molarity for both enantiomers is kept the same, then *e.e*% can be written in terms of solution volume V as

$$e.e\,\% = \left(\frac{V_- - V_+}{V_- + V_+}\right) * 100 \tag{12}$$

Subscripts + and − denote corresponding enantiomer. An *e.e*% of 0% indicates a racemic mixture, having 50% each of both enantiomers.

Before molecular adsorption, the sensor's surface is rinsed with acetone, IPA, and deionized water followed by blow-drying with nitrogen gas. It is then introduced in an O_2 plasma chamber for 2 min. This improves surface wettability. A PDMS cutout well is placed on the sensor for sample confinement. The prepared molecular solution is then drop-casted and spun-coated on the sensor surface at 800 rpm for 20 s and then gently warmed for 10 min. This creates a homogenous film of molecular coating on the region of interest. To maintain potency of thalidomide, the experiments are conducted within 24 hours of preparation of fresh thalidomide solutions from stored aliquots.

Experimental characterization

The detection setup schematic is shown in fig. S3B. The experimental setup consists of a reflection-based microscope (HYPERION 1000, Bruker Corp.) coupled to a FTIR spectroscopy system (VERTEX 80, Bruker Corp.). The spectrometer is configured with a MIR globar thermal source and a KBr beamsplitter. A broadband ZnSe linear polarizer (LP) with its fast axis along the horizontal direction is placed along the output of the FT-IR system's beam path. The light is redirected toward a motorized rotation stage (PRM1Z8, Thorlabs)–mounted achromatic (4000 to 1429 cm^{-1}) quarter-wave plate (QWP) (Bernhard Halle Nachfolger GmbH). The generated CPL is incident on the sensor surface, and the reflected response is redirected to a cryo-cooled MCT broadband infrared detector integrated within the microscope. The spectral response is measured for both right- and left-handed CPL excitation by rotation of the QWP to 45° and −45°, respectively, with respect to the LP axis. The final processing is performed with Bruker's spectra measuring and processing software OPUS.

Nano-FTIR measurement

The FTIR spectrum of adsorbed thin film thalidomide is collected using a commercial tip-based scattering-type scanning near-field optical microscopy (neaspec GmbH) system coupled to a fiber-based, broadband ultrafast laser (FemtoFiber dichro midIR, Toptica) spanning from 5 to 15 µm. The AFM-based system operates in tapping mode with a metal-coated Si tip operating at a tapping frequency of ~280 kHz and tapping amplitude of 60 nm at ambient conditions. The spatial resolution of the near-field signal is dictated by the AFM tip diameter of <20 nm. The tip-scattered signal is collected through a liquid N_2-cooled MCT detector and demodulated at the second harmonic of the tapping frequency to eliminate far-field background noise. The scattering amplitude (s) and phase (φ) are obtained through a pseudo-heterodyne technique based on an asymmetric Michelson interferometer (*54*). Simultaneous acquisition of amplitude and phase topography with height variation profile enables clear identification of thalidomide from the bare Au substrate and further obtain a nanoscale FTIR spectrum at the specific target location. The average thickness of the adsorbed thalidomide molecular layer is determined using the tapping-mode AFM module of the same system.

Reproducibility of results

Spectral measurements in the infrared range are very sensitive to temperature and humidity fluctuations and interfering gases. We perform our experiment in a controlled environment with regulated temperature where the humidity is typically <45%. Before beginning the measurements, the system is kept on standby for 20 min to allow the MIR source and detector to stabilize. During the experiment, the sample region is purged every 10 min with inert nitrogen gas to minimize CO_2 interference. Every measurement is averaged over 156 times to remove background noise fluctuations.

Before adsorption, the sensor is cleaned with acetone, IPA, and ionized water, dried with nitrogen followed by plasma cleaning in an O_2 plasma chamber. This improves the wettability of the gold surface. Every measurement of adsorbed enantiopure thalidomide is repeated five times, and the enantiomeric excess of thalidomide

solutions is repeated three times. In between every measurement, the sensor is sonicated in acetone for 5 min, followed by the cleaning protocol mentioned above.

During fabrication, the periodic surface is not always entirely uniform over the region of measurement (~0.5 mm by 0.5 mm in our case), which may introduce some nonzero CD reading for pristine sensors as well. To circumvent that, we coat the sensors with racemic mixtures of each measured thalidomide concentration. We then subtract this baseline from our original dissymmetry value to obtain the dissymmetry factor spectra reported in Fig. 3B.

The achromatic QWP used operates within the 2.5- to 7-μm (4000 to 1429 cm^{-1}) range. To minimize small inhomogeneity in uniform quarter-phase retardation over the broadband spectral range, separate baseline references are performed for RCP (+45° relative to polarizer) and LCP (−45° relative to polarizer) excitations on a gold reflective substrate, which are then used for subsequent corresponding normalized measurements of the adsorbed chiral analytes (RCP baseline for RCP excitation and LCP baseline for LCP excitation). The measured RCP and LCP reflectance spectra are then used to calculate the dissymmetry, which is now free from any retarder-induced artifacts. This guarantees that the excitation is mostly single-handed polarized for specific QWP angle.

Simulation modelling

For electromagnetic simulations of the near-field of the plasmonic system, we use FDTD (Lumerical FDTD) method that solves the Maxwell's equation numerically in time domain using the Yee cell method. Figure S1 (A and B) are the 2D far-field reflectance plots showing wavelength versus cavity thickness for RCP and LCP excitation, respectively, of the plasmonic system. Figure S1 (C, left) shows the reflectance plots corresponding to the dashed lines in fig. S1 (A and B) as well for linearly polarized excitation. The differential (RCP − LCP) value is shown in fig. S1 (C, right). The other geometric parameters are kept fixed (periodicity of 1740 nm, radius of 530 nm, and RD of 300 nm). The optical parameters (complex refractive indices) for gold and silicon dioxide are taken from experimentally determined data (*55*). The near-field electric and magnetic mode enhancement at the first-order LSPR at wavelength 5.41 μm is shown in fig. S1D for the reflectance graph shown in fig. S1A corresponding to the yellow dashed line on the 2D plot.

For simulating light-matter interaction for chiral layers, we use the use of COMSOL Multiphysics software, which is a FEM-based modeling software. In the "electromagnetic wave module in the frequency domain" module, we introduce a new "study" for wave equation and modify the consecutive relations for $\vec{D}$, $\vec{H}$ and $\frac{d\vec{H}}{dt}$ as per the relations mentioned in Eqs. 7 and 8. In contrast, the FDTD solver does not readily facilitate these modifications. For the three cases of left off-resonance, on-resonance, and right off-resonance, the geometry parameters of periodicity ($P = 1740$ nm), hole diameter ($D = 1060$ nm), and RD (= 300 nm) are all kept the same, while the cavity thickness (L) is changed to 800, 1000, and 1200 nm, respectively. The chiral molecule is simulated as a thin layer of 160 nm (which was verified by AFM profiling) with a dispersion relation for ε_r and κ given by the relations in Eqs. 6 and 7. The ω_0 and Γ, corresponding to the molecule's resonant frequency and damping coefficient, respectively, are extracted from the measured nano-FTIR spectra shown in fig. S3A. The background relative permittivity value ε_{r0} is taken from standard literature values for thalidomide. The other two parameters γ and β, which determine the amplitudes of absorptive and chiral properties of the molecule at resonance, respectively, are determined from fitting the simulation dissymmetry spectra to our experimental dissymmetry spectra results. Thus, the parameter values are chosen as $\varepsilon_{r0} = 2.341$, $\beta = 1.58 \times 10^{-4}$ eV, $\gamma = 1.22 \times 10^{-3}$ eV, and $\Gamma = 1.86 \times 10^{-3}$ eV, and it matches the resonant chiral response (ω_0) at 5.79 μm (1727 cm^{-1}). The κ value signifies the amount of inherent chiral response displayed by a chiral medium and is difficult to measure or estimate for a real system. However, at vibrational absorption resonances, where the dipole responses of the molecules are sensitive to the excitation, this value is several orders of magnitude higher than at off-resonant cases. In addition, considering that dense layer of molecules is adsorbed over the sensor's active surface and given that the coefficient β depends on the molecular density (*46*), κ in the order of 10^{-2} to 10^{-1} is reasonable at resonant wavelengths (*43*) compared to off-resonant values (10^{-6} to 10^{-5}). We varied κ and obtained good match with experimental observations.

Supplementary Materials

This PDF file includes:

Figs. S1 to S5

REFERENCES AND NOTES

1. L. A. Nguyen, H. He, C. Pham-Huy, Chiral drugs: An overview. *Int. J. Biomed. Sci.* **2**, 85–100 (2006).
2. J. H. Kim, A. R. Scialli, Thalidomide: The tragedy of birth defects and the effective treatment of disease. *Toxicol. Sci.* **122**, 1–6 (2011).
3. T. A. Keiderling, Protein and peptide secondary structure and conformational determination with vibrational circular dichroism. *Curr. Opin. Chem. Biol.* **6**, 682–688 (2002).
4. J. D. Jackson, *Classical Electrodynamics* (Wiley, ed. 3, 1998).
5. K. Y. Bliokh, F. Nori, Transverse and longitudinal angular momenta of light. *Phys. Rep.* **592**, 1–38 (2015).
6. D. M. Lipkin, Existence of a new conservation law in electromagnetic theory. *J. Math. Phys.* **5**, 696–700 (1964).
7. Y. Tang, A. E. Cohen, Optical chirality and its interaction with matter. *Phys. Rev. Lett.* **104**, 163901 (2010).
8. Y. Tang, A. E. Cohen, Enhanced enantioselectivity in excitation of chiral molecules by superchiral light. *Science* **332**, 333–336 (2011).
9. K. Y. Bliokh, F. Nori, Characterizing optical chirality. *Phys Rev A* **83**, 021803 (2011).
10. E. Hendry, T. Carpy, J. Johnston, M. Popland, R. V. Mikhaylovskiy, A. J. Lapthorn, S. M. Kelly, L. D. Barron, N. Gadegaard, M. Kadodwala, Ultrasensitive detection and characterization of biomolecules using superchiral fields. *Nat. Nanotechnol.* **5**, 783–787 (2010).
11. S. L. Prosvirnin, N. I. Zheludev, Polarization effects in the diffraction of light by a planar chiral structure. *Phys. Rev. E Stat. Nonlin. Soft Matter Phys.* **71** (3 Pt 2B), 037603 (2005).
12. A. S. Schwanecke, A. Krasavin, D. M. Bagnall, A. Potts, A. V. Zayats, N. I. Zheludev, Broken time reversal of light interaction with planar chiral nanostructures. *Phys. Rev. Lett.* **91**, 247404 (2003).
13. A. Papakostas, A. Potts, D. M. Bagnall, S. L. Prosvirnin, H. J. Coles, N. I. Zheludev, Optical manifestations of planar chirality. *Phys. Rev. Lett.* **90**, 107404 (2003).
14. M. Schäferling, N. Engheta, H. Giessen, T. Weiss, Reducing the complexity: Enantioselective chiral near-fields by diagonal slit and mirror configuration. *ACS Photonics* **3**, 1076–1084 (2016).
15. M. Schäferling, X. Yin, N. Engheta, H. Giessen, Helical plasmonic nanostructures as prototypical chiral near-field sources. *ACS Photonics* **1**, 530–537 (2014).
16. E. Hendry, R. V. Mikhaylovskiy, L. D. Barron, M. Kadodwala, T. J. Davis, Chiral electromagnetic fields generated by arrays of nanoslits. *Nano Lett.* **12**, 3640–3644 (2012).
17. M. Schäferling, D. Dregely, M. Hentschel, H. Giessen, Tailoring enhanced optical chirality: Design principles for chiral plasmonic nanostructures. *Phys. Rev. X* **2**, 031010 (2012).
18. M. Schäferling, X. Yin, H. Giessen, Formation of chiral fields in a symmetric environment. *Opt. Express* **20**, 26326–26336 (2012).
19. A. García-Etxarri, J. A. Dionne, Surface-enhanced circular dichroism spectroscopy mediated by nonchiral nanoantennas. *Phys. Rev. B* **87**, 235409 (2013).
20. T. J. Davis, E. Hendry, Superchiral electromagnetic fields created by surface plasmons in nonchiral metallic nanostructures. *Phys. Rev. B* **87**, 085405 (2013).

21. X. Tian, Y. Fang, M. Sun, Formation of enhanced uniform chiral fields in symmetric dimer nanostructures. *Sci. Rep.* **5**, 17534 (2015).
22. M. L. Solomon, J. Hu, M. Lawrence, A. García-Etxarri, J. A. Dionne, Enantiospecific optical enhancement of chiral sensing and separation with dielectric metasurfaces. *ACS Photonics* **6**, 43–49 (2019).
23. E. Pedrueza-Villalmanzo, F. Pineider, A. Dmitriev, Perspective: Plasmon antennas for nanoscale chiral chemistry. *Nanophotonics* **9**, 481–489 (2020).
24. L. A. Warning, A. R. Miandashti, L. A. McCarthy, Q. Zhang, C. F. Landes, S. Link, Nanophotonic approaches for chirality sensing. *ACS Nano* **15**, 15538–15566 (2021).
25. M. L. Nesterov, X. Yin, M. Schäferling, H. Giessen, T. Weiss, The role of plasmon-generated near fields for enhanced circular dichroism spectroscopy. *ACS Photonics* **3**, 578–583 (2016).
26. J. Mun, M. Kim, Y. Yang, T. Badloe, J. Ni, Y. Chen, C.-W. Qiu, J. Rho, Electromagnetic chirality: From fundamentals to nontraditional chiroptical phenomena. *Light Sci. Appl.* **9**, 139 (2020).
27. W. Liu, L. Deng, Y. Guo, W. Yang, S. Xia, W. Yan, Y. Yang, J. Qin, L. Bi, Enhanced chiral sensing in achiral nanostructures with linearly polarized light. *Opt. Express* **30**, 26306–26314 (2022).
28. F. Graf, J. Feis, X. Garcia-Santiago, M. Wegener, C. Rockstuhl, I. Fernandez-Corbaton, Achiral, helicity preserving, and resonant structures for enhanced sensing of chiral molecules. *ACS Photonics* **6**, 482–491 (2019).
29. J. Feis, D. Beutel, J. Köpfler, X. Garcia-Santiago, C. Rockstuhl, M. Wegener, I. Fernandez-Corbaton, Helicity-preserving optical cavity modes for enhanced sensing of chiral molecules. *Phys. Rev. Lett.* **124**, 033201 (2020).
30. A. Safaei, S. Modak, A. Vázquez-Guardado, D. Franklin, D. Chanda, Cavity-induced hybrid plasmon excitation for perfect infrared absorption. *Opt. Lett.* **43**, 6001–6004 (2018).
31. A. Safaei, S. Modak, J. Lee, S. Chandra, D. Franklin, A. Vázquez-Guardado, D. Chanda, Multi-spectral frequency selective mid-infrared microbolometers. *Opt. Express* **26**, 32931–32940 (2018).
32. A. Vázquez-Guardado, D. Chanda, Superchiral light generation on degenerate achiral surfaces. *Phys. Rev. Lett.* **120**, 137601 (2018).
33. C. Gilroy, S. Hashiyada, K. Endo, A. S. Karimullah, L. D. Barron, H. Okamoto, Y. Togawa, M. Kadodwala, Roles of superchirality and interference in chiral plasmonic biodetection. *J. Phys. Chem. C* **123**, 15195–15203 (2019).
34. R. Knipper, V. Kopecký Jr., U. Huebner, J. Popp, T. G. Mayerhöfer, Slit-enhanced chiral- and broadband infrared ultra-sensing. *ACS Photonics* **5**, 3238–3245 (2018).
35. Y. Zhao, A. N. Askarpour, L. Sun, J. Shi, X. Li, A. Alù, Chirality detection of enantiomers using twisted optical metamaterials. *Nat. Commun.* **8**, 14180 (2017).
36. C. Guo, R. D. Shah, R. K. Dukor, T. B. Freedman, X. Cao, L. A. Nafie, Fourier transform vibrational circular dichroism from 800 to 10,000cm^{-1}: Near-IR-VCD spectral standards for terpenes and related molecules. *Vib. Spectrosc.* **42**, 254–272 (2006).
37. A. Vázquez-Guardado, A. Safaei, S. Modak, D. Franklin, D. Chanda, Hybrid coupling mechanism in a system supporting high order diffraction, plasmonic, and cavity resonances. *Phys. Rev. Lett.* **113**, 263902 (2014).
38. D. Franklin, S. Modak, A. Vázquez-Guardado, A. Safaei, D. Chanda, Covert infrared image encoding through imprinted plasmonic cavities. *Light Sci. Appl.* **7**, 93 (2018).
39. A. Bamias, M. A. Dimopoulos, Thalidomide and immunomodulatory drugs in the treatment of cancer. *Expert Opin. Investig. Drugs* **14**, 45–55 (2005).
40. S. Singhal, J. Mehta, Thalidomide in cancer. *BioDrugs* **15**, 163–172 (2001).
41. G. V. Sherbet, Therapeutic potential of thalidomide and its analogues in the treatment of cancer. *Anticancer Res.* **35**, 5767–5772 (2015).
42. A. Dazzi, C. B. Prater, AFM-IR: Technology and applications in nanoscale infrared spectroscopy and chemical imaging. *Chem. Rev.* **117**, 5146–5173 (2017).
43. T. Iida, A. Ishikawa, T. Tanaka, A. Muranaka, M. Uchiyama, Y. Hayashi, K. Tsuruta, Super-chiral vibrational spectroscopy with metasurfaces for high-sensitive identification of alanine enantiomers. *Appl. Phys. Lett.* **117**, 101103 (2020).
44. A. H. Sihvola, A. J. Viitanen, I. V. Lindell, S. A. Tretyakov, *Electromagnetic Waves in Chiral and Bi-Isotropic Media* (Artech House Antenna Library, ed. 1, 1994).
45. J. García-Guirado, M. Svedendahl, J. Puigdollers, R. Quidant, Enhanced chiral sensing with dielectric nanoresonators. *Nano Lett.* **20**, 585–591 (2020).
46. N. A. Abdulrahman, Z. Fan, T. Tonooka, S. M. Kelly, N. Gadegaard, E. Hendry, A. O. Govorov, M. Kadodwala, Induced chirality through electromagnetic coupling between chiral molecular layers and plasmonic nanostructures. *Nano Lett.* **12**, 977–983 (2012).
47. A. O. Govorov, Z. Fan, Theory of chiral plasmonic nanostructures comprising metal nanocrystals and chiral molecular media. *ChemPhysChem* **13**, 2551–2560 (2012).
48. K. Yao, Y. Liu, Enhancing circular dichroism by chiral hotspots in silicon nanocube dimers. *Nanoscale* **10**, 8779–8786 (2018).
49. E. Mohammadi, K. L. Tsakmakidis, A. N. Askarpour, P. Dehkhoda, A. Tavakoli, H. Altug, Nanophotonic platforms for enhanced chiral sensing. *ACS Photonics* **5**, 2669–2675 (2018).
50. R. Adato, A. A. Yanik, J. J. Amsden, D. L. Kaplan, F. G. Omenetto, M. K. Hong, S. Erramilli, H. Altug, Ultra-sensitive vibrational spectroscopy of protein monolayers with plasmonic nanoantenna arrays. *Proc. Natl. Acad. Sci. U.S.A.* **106**, 19227–19232 (2009).
51. F. Cheng, X. Yang, J. Gao, Ultrasensitive detection and characterization of molecules with infrared plasmonic metamaterials. *Sci. Rep.* **5**, 14327 (2015).
52. F. Neubrech, A. Pucci, T. W. Cornelius, S. Karim, A. García-Etxarri, J. Aizpurua, Resonant plasmonic and vibrational coupling in a tailored nanoantenna for infrared detection. *Phys. Rev. Lett.* **101**, 157403 (2008).
53. R. Adato, A. Artar, S. Erramilli, H. Altug, Engineered absorption enhancement and induced transparency in coupled molecular and plasmonic resonator systems. *Nano Lett.* **13**, 2584–2591 (2013).
54. N. Ocelic, A. Huber, R. Hillenbrand, Pseudoheterodyne detection for background-free near-field spectroscopy. *Appl. Phys. Lett.* **89**, 101124 (2006).
55. E. D. Palik, *Handbook of Optical Constants of Solids* (Academic Press, 1998), vol. 3.

Acknowledgments

Funding: This work at the University of Central Florida was supported by NSF grant no. ECCS-1800845. **Author contributions:** Conceptualization: A.B., M.W.S., and D.C. Investigation: A.B. and M.K. Methodology: A.B., M.W.S., and D.C. Resources: A.B., M.K., and D.C. Funding acquisition: D.C. Data curator: A.B., M.K., and D.C. Validation: A.B., M.W.S., M.K., and D.C. Supervision: A.B., P.C.-A., and D.C. Formal analysis: A.B. and M.W.S. Software: A.B. and M.W.S. Project administration: A.B., P.C.-A., and D.C. Visualization: A.B., M.K., and D.C. Writing—original draft: A.B. and D.C. Writing—reviewing and editing: A.B., P.C.-A., M.W.S., and D.C. **Competing interests:** The authors declare that they have no competing interests. **Data and materials availability:** All data needed to evaluate the conclusions in the paper are present in the paper and/or the Supplementary Materials.

Submitted 22 August 2023
Accepted 22 January 2024
Published 23 February 2024
10.1126/sciadv.adk2560